nature physics

LETTERS

https://doi.org/10.1038/s41567-018-0213-x

Topological spin excitations in a three-dimensional antiferromagnet

Weiliang Yao[1,9], Chenyuan Li[1,9], Lichen Wang[1,9], Shangjie Xue[1], Yang Dan[1,7], Kazuki Iida[2], Kazuya Kamazawa[2], Kangkang Li[3,4,8], Chen Fang[3,5*] and Yuan Li[1,6*]

Band topology, namely the global wavefunction structure that gives rise to the properties observed in the bulk and on the surface of crystalline materials, is currently a topic under intense investigation for both fundamental interest and its technological potential[1–4]. While topological band crossing in three dimensions was first studied for electrons in semimetals[4–10], the underlying physical idea is not restricted to fermions[11–15] and similar band structures of electromagnetic waves have been observed in artificial structures[16]. Fundamental bosonic excitations in real crystals, however, have not been observed to exhibit any counterparts. Here we use inelastic neutron scattering to reveal the presence of topological spin excitations (magnons) in a three-dimensional antiferromagnet, Cu_3TeO_6, which features a unique lattice of magnetic spin-1/2 Cu^{2+} ions[17]. Further to previous works on this system[17,18], we find that the Cu^{2+} spins interact over a variety of distances, with the ninth-nearest-neighbour interaction being particularly strong. While the presence of topological magnon band crossing is independent of model details[15], the far-reaching interactions suppress quantum fluctuations and make the magnon signals sharp and intense. Using accurate measurement and calculation, we visualize two magnon bands that cross at Dirac points protected by (approximate) U(1) spin-rotation symmetry. As a limiting case of topological nodal lines with Z_2-monopole charges[15,19], these Dirac points are new to the family of experimentally confirmed topological band structures. Our results render magnon systems a fertile ground for exploring novel band topology with neutron scattering, along with distinct observables in other related experiments.

Magnons are quantized spin-1 excitations from an ordered magnetic ground state. Unlike electrons, where the topological band crossings must be below the Fermi energy for momentum-resolved observation with photoemission, there is not a similar constraint on the energy level of magnons. However, many magnetic materials have too few spins in the primitive cell to allow for any magnon band crossing at all. It was previously envisioned that topological magnon band crossing in the form of Weyl points would be possible only in the restrictive cases of non-centrosymmetric crystal structures[13] or certain types of ferromagnet[14]. Meanwhile, the magnetic space groups[20] are considerably more complicated than the crystallographic space groups[21–23], and symmetry requirements for stabilizing Dirac-point-like band crossings[7] have not been determined. Recently, some of us proposed that topological magnon band crossing may occur in antiferromagnets[15] with *PT* (time reversal followed by space inversion) symmetry. This unlocks far more materials to be considered than previously thought.

As an insulator, Cu_3TeO_6 develops antiferromagnetic order below the Néel temperature $T_N = 61$ K (Supplementary Fig. 1). The order features a bipartite and predominantly collinear arrangement[17] of spin-1/2 on the Cu^{2+} sublattice (Fig. 1a). Figure 2 presents spin excitation signals measured with inelastic neutron scattering (INS) in and out of the magnetically ordered state. Well-defined magnons are observed at 4 K (Fig. 2a), and they have collapsed into a featureless cloud of excitations at 73 K (Fig. 2b,d), which is not far above T_N. At 4 K, a total of 6 magnon branches are observed, suggesting that they are all doubly degenerate (since the primitive cell has 12 Cu^{2+} ions) and that the spin Hamiltonian has U(1) spin-rotation symmetry[15]. However, this can be only approximately true, because we do observe a small gap at the bottom of the 'acoustic' branch (Fig. 2e,f). Since exact cubic (or tetrahedral) symmetry precludes a global magnetic easy axis, the gap can be ascribed to the presence of Dzyaloshinsky–Moriya interactions and hence the lack of U(1) symmetry. We will revisit this point later.

Our highly extensive INS data allow us to determine the magnon spectra over many Brillouin zones (BZs, Fig. 2c), in which we expect a different dynamic structure factor $S(\mathbf{Q},\omega)$ but the same dispersion $\omega_m(\mathbf{q})$. Here, $\mathbf{Q}$ and ω are respectively the momentum and energy transfers of the scattering, m is the magnon branch index and $\mathbf{q}$ is the displacement of $\mathbf{Q}$ from the nearest BZ centre. Figure 3a–c displays INS data recorded along three sets of high-symmetry lines in $\mathbf{Q}$ space. The data are free from phonon contributions, which become noticeable only in higher BZs (Supplementary Fig. 2).

Before we proceed to the modelling of our INS data and the analysis of the band topology, we note that magnetic INS signals are not always clear and sharp. Poor sample mosaic, crystal defects, thermal broadening and instrumental resolution all contribute to the experimental linewidth. For antiferromagnets, the intrinsic linewidth (even in perfect crystals at zero temperature) is further increased by quantum fluctuations[24] that are strong in systems with reduced dimensionality, frustrated interactions and small spins. In fact, quantum fluctuations can be as severe as causing magnons to

[1]International Centre for Quantum Materials, School of Physics, Peking University, Beijing, China. [2]Neutron Science and Technology Centre, Comprehensive Research Organization for Science and Society (CROSS), Tokai, Japan. [3]Beiijng National Laboratory for Condensed Matter Physics, and Institute of Physics, Chinese Academy of Sciences, Beijing, China. [4]University of Chinese Academy of Sciences, Beijing, China. [5]CAS Centre for Excellence in Topological Quantum Computation, Beijing, China. [6]Collaborative Innovation Centre of Quantum Matter, Beijing, China. [7]Present address: Department of Materials Science and Engineering, University of Illinois at Urbana-Champaign, Champaign, IL, USA. [8]Present address: Department of Physics, The University of Hong Kong, Hong Kong, China. [9]These authors contributed equally: Weiliang Yao, Chenyuan Li, Lichen Wang. *e-mail: cfang@iphy.ac.cn; yuan.li@pku.edu.cn

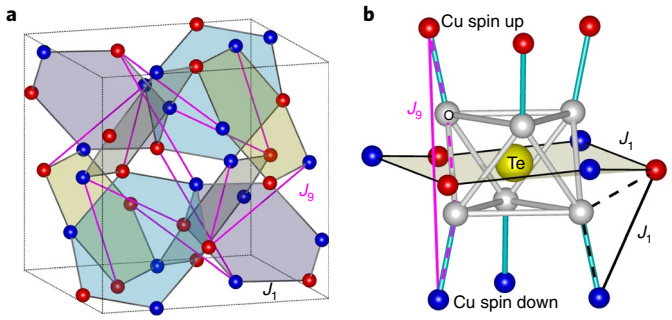

Fig. 1 | Primary magnetic interactions in Cu_3TeO_6. a, The magnetic lattice shown in a cubic unit cell that contains two primitive cells and eight formula units. Cu_3TeO_6 belongs to the cubic space group *Ia*-3 (no. 206; $a = 9.537$ Å), and its collinear magnetic ground state assumed here belongs to the magnetic space group *R*-3′ (no. 148.19). Spin-up and spin-down Cu^{2+} are represented in different colours. The nearest-neighbour (J_1) and the ninth-nearest-neighbour (J_9) interactions constitute a highly interconnected network. **b**, Exchange pathways (dashed lines) of J_1 and J_9 via oxygen atoms. The relatively straight pathway of J_9 makes it comparable to J_1, despite the greater distance.

disintegrate into fractionalized 'spinon' excitations in one[25] and two dimensions[26,27]. Such quantum effects render the prediction of topological magnon band structures[13–15] based on a harmonic, non-interacting picture of the magnons potentially questionable. The above considerations appear to challenge the proposal[15] that Cu_3TeO_6 is a candidate material for the observation of topological magnons. The apparent difficulty is that each Cu^{2+} has only four nearest neighbours connected by the antiferromagnetic interaction J_1; that is, the coordination number ($N = 4$) is the same as in a two-dimensional square lattice[18]. Even though a second-nearest-neighbour interaction (J_2) might exist, it is expected to be weak, as otherwise the magnetic lattice becomes frustrated[17]. Moreover, spin-1/2 is the extreme case for strong quantum fluctuations.

In contrast to these concerns, the INS data in Figs. 2a and 3a–c consistently indicate highly coherent quasiparticles throughout the magnon band width, which invites a harmonic modelling of the spin dynamics. To this end, we employ linear spin-wave theory (LSWT), which is by far the most commonly used method for calculating magnons. We assume that LSWT offers an effective account for the microscopic harmonic spin Hamiltonian, so that if it successfully models the data, the harmonic description is considered justified, and the band topology can be faithfully represented by its results as a motivational principle. We have applied a two-step modelling approach to the INS data. In the first step, we only estimate the effective spin interactions (J terms) and anisotropy by fitting the experimental $\omega_m(\mathbf{q})$, which we obtain by inspection (Supplementary Figs. 3a and 4). This step is useful for avoiding a blind parameter search directly based on $S(\mathbf{Q},\omega)$, and it becomes clear already in this step that interactions up to J_9, the interaction between the ninth-nearest neighbours, are necessary (see Methods). In the second step, we fit the $S(\mathbf{Q},\omega)$ patterns in Fig. 3b by introducing two more parameters: an overall intensity coefficient and effective damping (see Methods). Optimizing all parameters results in modest updates to the values of J terms (Supplementary Table 1). The excellent agreement (Fig. 3 and Supplementary Fig. 4) between

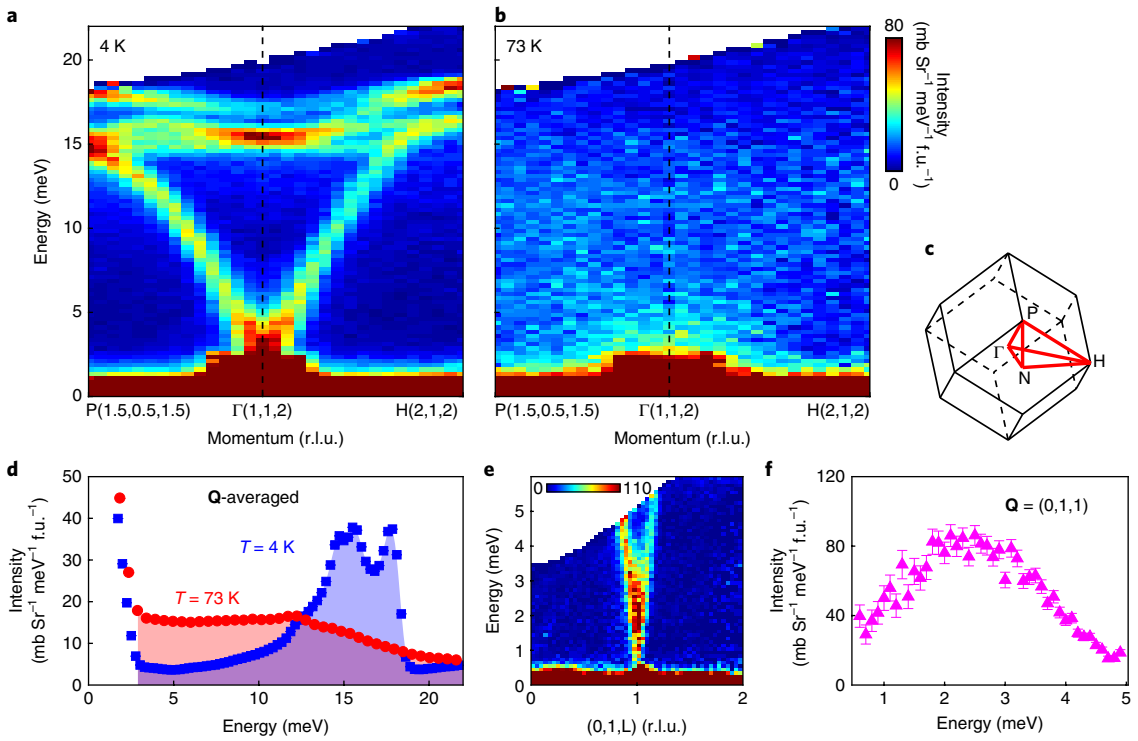

Fig. 2 | Basic properties of spin excitations. a,**b**, Representative INS data taken with incident neutron energy $E_i = 28$ meV in the ordered and the paramagnetic states, respectively. The data are shown near a magnetic ordering wavevector $\mathbf{Q} = (1,1,2)$ (in reciprocal lattice units, r.l.u.). **c**, The BZ, with high-symmetry lines indicated in red. **d**, Energy distribution of INS intensities averaged over more than ten BZs. The total spectral weights (shaded areas), mostly magnetic, are the same at both temperatures within 2% accuracy. **e**,**f**, Data near the bottom of the acoustic magnon branch, measured at 4 K with $E_i = 8$ meV, indicating a small gap of about 2 meV. All measured intensities are displayed in absolute cross-section units (see Methods), and the error bars indicate statistical uncertainty (1 s.d.).

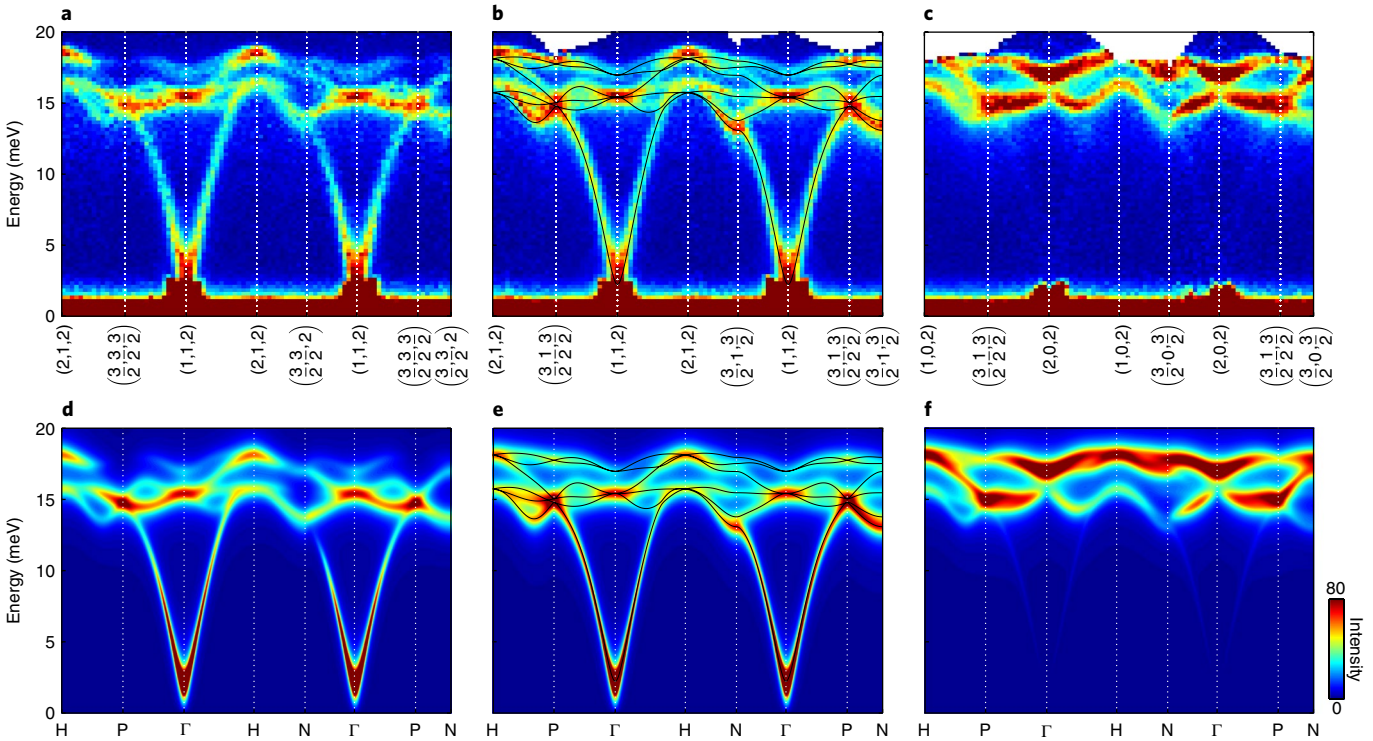

Fig. 3 | Comparison between INS and LSWT-calculated magnon spectra. a–c, INS intensities along three momentum trajectories, measured at 4 K with $E_i = 28$ meV. **d–f**, Calculated $S(\mathbf{Q},\omega)$ along the same trajectories as in **a–c** using the optimized parameter set. An effective anisotropy parameter is needed to describe the acoustic branch, but it does not affect the description of the optical branches (see Supplementary Fig. 3). All measured and calculated intensities are displayed in the same absolute units (see Methods) after Fig. 2. The solid lines in **b** and **e** indicate the (same) calculated magnon dispersions, which apply to all panels.

our LSWT results (with 12 adjustable parameters) and the INS data (raw-format data > 30 GB, reduced to about 300 kB for plotting in Fig. 3) indicates that our LSWT model provides an excellent effective account for the spin excitations in Cu_3TeO_6.

The fitting parameters (see Supplementary Table 1) indicate that the magnetic interactions are dominated by antiferromagnetic J_9 and J_1 with very similar strengths. Although surprising at first sight, the prominence of J_9 can be understood as originating from a strong super-superexchange interaction[28] on the relatively straight bond sequence Cu–O–O–Cu (Fig. 1b). Additional analyses of the exchange interactions are presented in Supplementary Fig. 5 and Supplementary Table 1. With $J_1 \approx J_9$, the spin lattice is highly interconnected ($N = 8$) without frustration (Fig. 1a), so quantum fluctuations are strongly suppressed. This further justifies the use of the LSWT modelling.

According to the general theory[15], the P-point of the BZ (Fig. 2c) is always a topological crossing point (a Dirac point, DP) when the system has U(1) symmetry. These DPs are indeed found in our calculated dispersions (Fig. 4a, solid lines): the six doubly degenerate bands cross at three DPs located at the P-point at different energies. Two of them are too close together near 15 meV for a reliable determination (Supplementary Fig. 6). Therefore, we focus here on the DP at about 17.8 meV involving the topmost two magnon bands, which can be more clearly resolved.

We first compare INS spectra measured along momentum cuts that have the same $\omega_m(\mathbf{q})$ but different $S(\mathbf{Q},\omega)$, to utilize the contrast in $S(\mathbf{Q},\omega)$ to better identify (or verify) the underlying dispersions. Figure 4a,b presents cuts connecting a P-point to two of its neighbouring H-points. In both the measurement and the calculation, the two bands near 18 meV are equally intense as **Q** moves from P(1.5,0.5,1.5) towards H(1,0,2), whereas only the high-energy band is pronounced as **Q** moves towards H(2,1,2). This results in a distinct envelope of the signal, indicated by the magenta dotted lines in Fig. 4a,b. Similar comparisons when moving **Q** in other pairs of equivalent directions are displayed in Supplementary Fig. 7, all indicating that there are two bands crossing at P without opening a gap.

A key signature of a DP is the nearby linear dispersions. To verify this, we turn to intensity patterns recorded in **Q** planes that connect a P-point to its neighbouring N-points (bottom of Fig. 4c). Our LSWT calculation predicts that the dispersions in this plane are four-fold symmetric about P with relatively high velocities (Fig. 4e), so that away from P the two bands differ by more than 0.5 meV (Fig. 4d) and should become marginally resolvable (our resolution is about 0.58 meV near 18 meV). In Fig. 4c, we show that such sub-resolution structures are indeed observed, after we combine and symmetrize all available data round P(1.5,0.5,1.5) (see captions for details). The linear dispersions can be further checked by organizing the INS data into energy distribution curves (EDCs). Figure 4f displays EDCs at a series of **Q**s along the trajectory indicated in Fig. 4d. Fitting all of the EDCs collectively, assuming the presence of two peaks away from P, results in an X-shaped dispersion. However, even if we were to fit the EDCs with a single peak, we still come to the same conclusion, as the peak width becomes broader away from P in a fashion that suggests sub-resolution DP-like dispersions. Additional EDCs are presented in Supplementary Figs. 8 and 9, all supporting this understanding. On the basis of this highly consistent set of evidence, we conclude that the characteristic dispersions near the DP are confirmed in our experiment.

The topological nature of the band crossing at the DPs can be verified beyond the linear dispersions. Using magnon eigenvectors calculated with our LSWT model, we confirm that the DPs indeed have non-trivial topological charges (Supplementary Fig. 6).

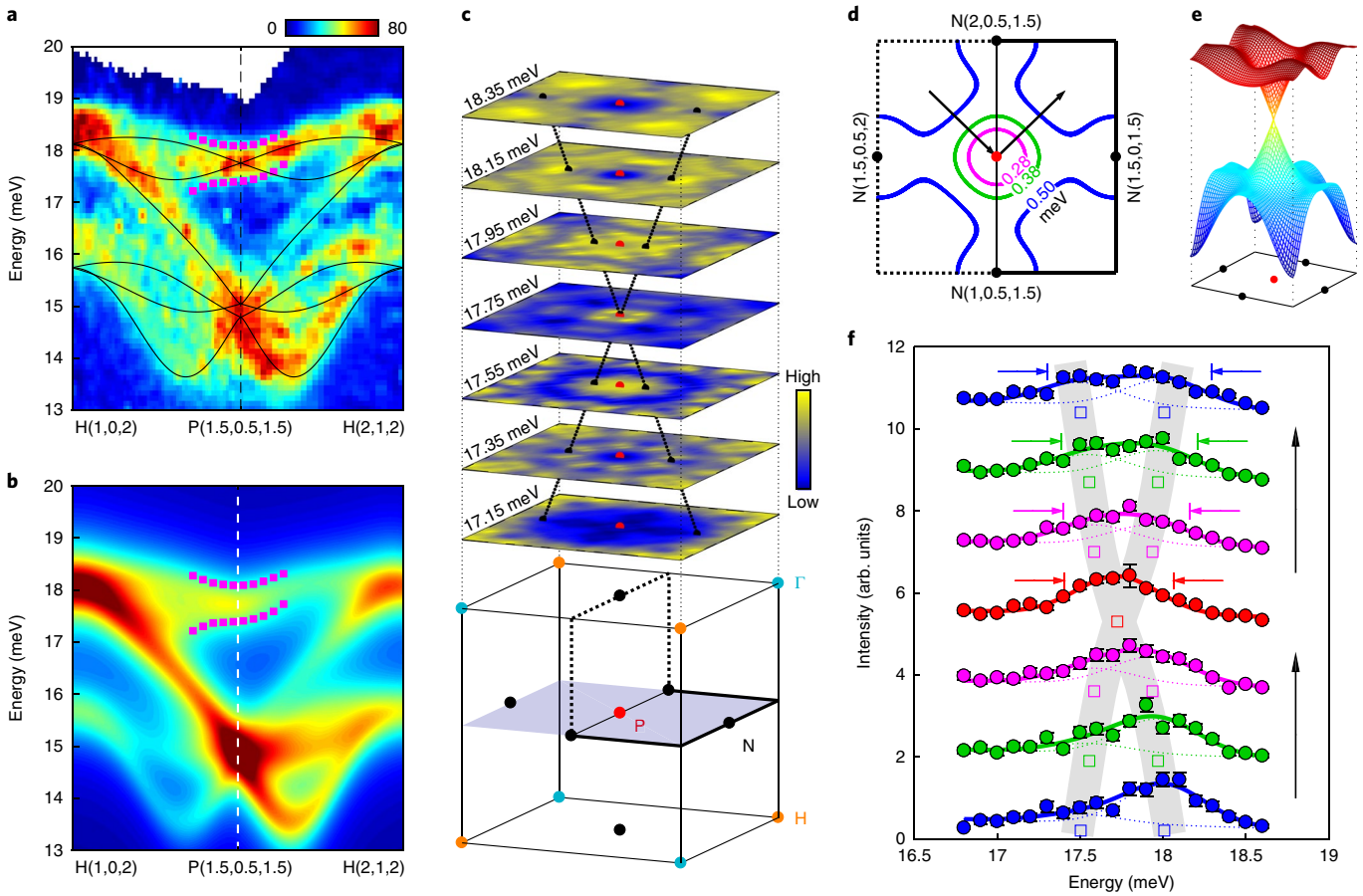

Fig. 4 | Evidence for Dirac-point-like magnon band crossing. a,**b**, INS and calculated $S(\mathbf{Q},\omega)$, respectively, along an H–P–H momentum trajectory. The solid lines indicate LSWT-calculated dispersions, and the magenta dotted lines indicate a characteristic intensity envelope (see text) identical between the two panels. Both the measured and calculated intensities are displayed in the same absolute units (see Methods) after Fig. 2. **c**, INS intensity distribution in 0.2 meV intervals in **Q**-space planes that connect P with its four neighbouring N-points (P–N planes). To enhance the visibility of sub-resolution structures, data from all available P–N planes (see Supplementary Fig. 11) are included and symmetrized around P(1.5,0.5,1.5). For each energy interval, the intensities are false-colour rendered with respect to their own maximum and minimum. The dotted lines in the upper part are a guide to the eye for illustrating the Dirac-cone-like structure. **d**, LSWT-calculated **Q** contours in the (90°-folded) P–N plane displayed in **c**, with indicated constant energy distances between the topmost two magnon bands. **e**, LSWT-calculated dispersions of the topmost two magnon bands in the P–N plane. **f**, EDCs of INS data at **Q** positions corresponding to the intersections between the arrows and the contours in **d**, colour-coded with the contours and offset for clarity. The vertical error bars indicate statistical uncertainties (1 s.d.), and are comparable to the size of the symbols for most of the data points. The solid and dotted lines are two-peak fits to the data and the individual peak components, respectively, obtained under the constraint that equivalent **Q** positions must have the same peak energies (open squares). Pairs of horizontal arrows indicate full-widths at half-maximum of the top four EDCs when fitted with a single peak (fits not shown), from the top: 0.99(7), 0.83(6), 0.77(6) and 0.66(5) meV, where the uncertainty (in parenthesis) corresponds to 1 s.d.

Moreover, as the eigenvectors are represented by the structures of $S(\mathbf{Q},\omega)$, the similarity between the measured and the calculated spectra (Fig. 4a,b and Supplementary Fig. 7) in the vicinity of the DPs can be taken as evidence for the non-trivial band topology. Last but not least, we expect magnon 'surface-arc' states to arise from the non-trivial band topology[15]. Indeed, as the bulk of Cu_3TeO_6 hosts a wealth of topological DPs beyond our above demonstration, the calculated surface-arc states are also extremely rich (Supplementary Fig. 10).

Given the topological magnon band structure, we expect the presence of topological Hall effects on magnon currents, which may enable novel spintronics (or 'magnonics') applications. The topological surface states can be probed by techniques that require only a small sample volume, such as high-resolution electron energy-loss spectroscopy (EELS) and resonant inelastic X-ray scattering (RIXS). Although the energy scale of Cu_3TeO_6 presents a challenge even to the best EELS and RIXS resolutions available at present, now that we have verified the general principles, new opportunities may arise as the techniques are improved and new materials discovered. Moreover, the surface states have a different energy distribution from the bulk states (Supplementary Fig. 10f), so even a carefully designed INS experiment on fine-powder samples of Cu_3TeO_6 (that is, with a large surface volume) might be able to detect them.

The DPs that we have observed are the limiting case of nodal lines that carry Z_2 topological monopole charges[15,19]. This limiting case requires U(1) symmetry, which is in principle absent in Cu_3TeO_6. Nonetheless, neglecting U(1) symmetry-breaking interactions, as we have done in our LSWT model, must be a very good approximation because their effect, namely, to expand each DP into a nodal line[15], occurs only in the second and higher order. Finding sizable such nodal lines in other materials will be interesting, and magnon systems are superior to electron systems for finding them: electron bands are typically detected (for example, by angle-resolved photoemission spectroscopy) with limited **Q** resolution perpendicular to the exposed surface, whereas magnons can be probed by INS with excellent resolution in all dimensions. Moreover, for electron bands

to have such nodal lines, the *PT* symmetry is required in conjunction with the absence of spin–orbit coupling, which is never strictly true[19]. Only the *PT* symmetry is required for magnons.

On top of this minimal requirement, additional symmetries, such as in the case of Cu_3TeO_6 here, may bring intriguing features to the magnon bands that deserve further investigation. The symmetry-enforced DPs (with U(1)) at the two P-points can be shown to have the same topological charges[15], so their presence necessitates the existence of additional DPs elsewhere in the BZ, as is reaffirmed by the rich surface-arc states (Supplementary Fig. 10). Moreover, we discover a 'sum rule' of magnon energies at high symmetry points of the BZ: $\sum_m(\omega^2_{\Gamma,m}+4\omega^2_{P,m}+\omega^2_{H,m})=\sum_m 6\omega^2_{N,m}$, which imposes constraints on how the bands may cross into one another. The sum rule holds exactly in the LSWT (for models with at least nine *J* terms), and to a precision of about 1% in our measured dispersions. At present, we do not know the precise origin of the sum rule, but we believe that it must be related to the space-group symmetry of the entire lattice and the site symmetry of Cu^{2+}. A close-knit comparison between real- and reciprocal-space pictures has led to recent progress in the understanding of electronic band topology[29,30], where the high symmetry of Cu_3TeO_6 has been noted as an extreme case of interconnected bands[29]. A counterpart analysis for magnon states in the magnetic groups[20] may lead to new insights for the prediction of novel magnon systems.

Note added in proof: Recently, ref. [31] appeared, which has some overlap with the present work. The main experimental results and interpretation of the two studies are consistent with each other.

Methods

Methods, including statements of data availability and any associated accession codes and references, are available at https://doi.org/10.1038/s41567-018-0213-x.

Received: 25 August 2017; Accepted: 15 June 2018;
Published online: 16 July 2018

References

1. Bansil, A., Lin, H. & Das, T. Colloquium: Topological band theory. *Rev. Mod. Phys.* **88**, 021004 (2016).
2. Chiu, C.-K., Teo, J. C. Y., Schnyder, A. P. & Ryu, S. Classification of topological quantum matter with symmetries. *Rev. Mod. Phys.* **88**, 035005 (2016).
3. Burkov, A. A. Topological semimetals. *Nat. Mater.* **15**, 1145–1148 (2016).
4. Armitage, N. P., Mele, E. J. & Vishwanath, A. Weyl and Dirac semimetals in three dimensional solids. *Rev. Mod. Phys.* **90**, 015001 (2018).
5. Murakami, S. Phase transition between the quantum spin Hall and insulator phases in 3D: emergence of a topological gapless phase. *New J. Phys.* **9**, 356 (2007).
6. Wan, X., Turner, A. M., Vishwanath, A. & Savrasov, S. Y. Topological semimetal and Fermi-arc surface states in the electronic structure of pyrochlore iridates. *Phys. Rev. B* **83**, 205101 (2011).
7. Young, S. M. et al. Dirac semimetal in three dimensions. *Phys. Rev. Lett.* **108**, 140405 (2012).
8. Liu, Z. K. et al. Discovery of a three-dimensional topological Dirac semimetal, Na_3Bi. *Science* **343**, 864–867 (2014).
9. Xu, S. Y. et al. Discovery of a Weyl fermion semimetal and topological Fermi arcs. *Science* **349**, 613–617 (2015).
10. Lv, B. Q. et al. Experimental discovery of Weyl semimetal TaAs. *Phys. Rev. X* **5**, 031013 (2015).
11. Lu, L., Joannopoulos, J. D. & Soljačić, M. Topological photonics. *Nat. Photon.* **8**, 821–829 (2014).
12. Stenull, O., Kane, C. L. & Lubensky, T. C. Topological phonons and Weyl lines in three dimensions. *Phys. Rev. Lett.* **117**, 068001 (2016).
13. Li, F. Y. et al. Weyl magnons in breathing pyrochlore antiferromagnets. *Nat. Commun.* **7**, 12691 (2016).
14. Mook, A., Henk, J. & Mertig, I. Tunable magnon Weyl points in ferromagnetic pyrochlores. *Phys. Rev. Lett.* **117**, 157204 (2016).
15. Li, K., Li, C., Hu, J., Li, Y. & Fang, C. Dirac and nodal line magnons in three-dimensional antiferromagnets. *Phys. Rev. Lett.* **119**, 247202 (2017).
16. Lu, L. et al. Experimental observation of Weyl points. *Science* **349**, 622–624 (2015).
17. Herak, M. et al. Novel spin lattice in Cu_3TeO_6: an antiferromagnetic order and domain dynamics. *J. Phys. Condens. Matter* **17**, 7667–7679 (2005).
18. Månsson, M. et al. Magnetic order and transitions in the spin-web compound Cu_3TeO_6. *Phys. Procedia* **30**, 142–145 (2012).
19. Fang, C., Chen, Y., Kee, H. Y. & Fu, L. Topological nodal line semimetals with and without spin-orbital coupling. *Phys. Rev. B* **92**, 081201(R) (2015).
20. Watanabe, H., Po, H. C. & Vishwanath, A. Structure and topology of band structures in the 1651 magnetic space groups. Preprint at https://arxiv.org/abs/1707.01903 (2017).
21. Bradlyn, B. et al. Beyond Dirac and Weyl fermions: Unconventional quasiparticles in conventional crystals. *Science* **353**, aaf5037 (2016).
22. Watanabe, H., Po, H. C., Zaletel, M. P. & Vishwanath, A. Filling-enforced gaplessness in band structures of the 230 space groups. *Phys. Rev. Lett.* **117**, 096404 (2016).
23. Bzdušek, T., Wu, Q., Rüegg, A., Sigrist, M. & Soluyanov, A. A. Nodal-chain metals. *Nature* **538**, 75–78 (2016).
24. Zhitomirsky, M. E. & Chernyshev, A. L. Colloquium: Spontaneous magnon decays. *Rev. Mod. Phys.* **85**, 219–243 (2013).
25. Lake, B., Tennant, D. A., Frost, C. D. & Nagler, S. E. Quantum criticality and universal scaling of a quantum antiferromagnet. *Nat. Mater.* **4**, 329–334 (2005).
26. Headings, N. S., Hayden, S. M., Coldea, R. & Perring, T. G. Anomalous high-energy spin excitations in the high-T_c superconductor-parent antiferromagnet La_2CuO_4. *Phys. Rev. Lett.* **105**, 247001 (2010).
27. Dalla Piazza, B. et al. Fractional excitations in the square lattice quantum antiferromagnet. *Nat. Phys.* **11**, 62–68 (2015).
28. Whangbo, M. H., Koo, H. J. & Dai, D. Spin exchange interactions and magnetic structures of extended magnetic solids with localized spins: theoretical descriptions on formal, quantitative and qualitative levels. *J. Solid State Chem.* **176**, 417–481 (2003).
29. Bradlyn, B. et al. Topological quantum chemistry. *Nature* **547**, 298–305 (2017).
30. Po, H. C., Vishwanath, A. & Watanabe, H. Complete theory of symmetry-based indicators of band topology. *Nat. Commun.* **8**, 50 (2017).
31. Bao, S. et al. Observation of Dirac magnons in a three-dimensional antiferromagnet Cu_3TeO_6. Preprint at https://arxiv.org/abs/1711.02960 (2017).

Acknowledgements

We wish to thank F. Wang, G. Chen, O. Janson, X. Zhang, E. Motoyama and L. Fu for discussions and comments. The INS experiments were performed at the MLF, J-PARC, Japan, under a user programme (proposal nos 2016B0116 and 2017I0001). Work at the Institute of Physics, Chinese Academy of Sciences is supported by the Ministry of Science and Technology of China (grant no. 2016YFA0302400) and the National Natural Science Foundation of China (grant no. 11674370). Work at Peking University is supported by the National Natural Science Foundation of China (grant no. 11522429) and the Ministry of Science and Technology of China (grant nos 2018YFA0305602 and 2015CB921302).

Author contributions

Y.L. conceived the research. L.W., C.L., C.F. and Y.L. designed the experiment. W.Y., C.L., L.W. and Y.D. prepared the sample. W.Y., C.L., S.X., K.I., K.K. and Y.L. performed the INS experiments. W.Y. and Y.L. analysed the experimental data. C.L., K.L. and C.F. performed the theoretical analyses. W.Y., C.L., L.W., C.F. and Y.L. wrote the paper with input from all co-authors.

Competing interests

The authors declare no competing interests.

Additional information

Supplementary information is available for this paper at https://doi.org/10.1038/s41567-018-0213-x.

Reprints and permissions information is available at www.nature.com/reprints.

Correspondence and requests for materials should be addressed to C.F. or Y.L.

Publisher's note: Springer Nature remains neutral with regard to jurisdictional claims in published maps and institutional affiliations.

Methods

Sample growth and characterization. High-quality single crystals of Cu_3TeO_6 were grown by a flux method using molten $PbCl_2$ as a solvent[32]. X-ray Laue backscattering from natural crystal surfaces produces sharp diffraction patterns with an approximate four-fold symmetry (Supplementary Fig. 1a), consistent with the cubic space group *Ia*-3 (no. 206; $a=9.537$ Å)[17]. For the INS experiments, we co-aligned about 80 pieces of single crystals by gluing them on aluminium plates using a hydrogen-free adhesive, amounting to a total crystal mass of about 16.8 g (Supplementary Fig. 1a). The entire array has a total mosaic spread of about 2°, as determined from the full-widths at half-maximum of rocking curves measured on the (0,0,3) and (2,2,0) Bragg reflections (Supplementary Fig. 1b). Temperature-dependent intensities of the magnetic Bragg reflection (1,1,0), as well as uniform magnetic susceptibility, indicate a sharp antiferromagnetic transition below $T_N=61$ K (Supplementary Fig. 1c,d). Fitting the high-temperature susceptibility data suggests a Curie–Weiss temperature of about −165 K, consistent with previous results[17].

INS experiments. Our INS experiments were performed on the 4SEASONS time-of-flight spectrometer at the MLF, J-PARC, Japan[33]. The spectrometer has a multiple-E_i capability[34], so that data in different energy ranges (with different energy resolutions) can be obtained simultaneously. All data presented were obtained with two chopper conditions: primary incident energy $E_i=28$ meV with chopper frequency 250 Hz (low resolution), and primary $E_i=31$ meV with chopper frequency 400 Hz (high resolution). Two different sample orientations were used in our measurements, with a crystallographic direction of either (1,0,0) or (1,1,0) being placed in the vertical direction. During the measurement, the sample is rotated about the vertical axis over a range of 180° in steps of 0.5°, and data accumulated at each angle were combined together, forming a four-dimensional data set, which we used the Utsusemi[35] and Horace[36] software packages to reduce and analyse. After a careful alignment of the measured data set with the crystallographic coordinate system using all available nuclear Bragg reflections, the entire data set was down-folded in the three-dimensional momentum space using the full cubic symmetry (T_h point group, plus four-fold rotations about the <100> directions; the four-fold rotational 'symmetries' were introduced by twinning during the crystal growth and the co-alignment processes). The folding resulted in a data volume that is 1/48 of the original, and it greatly enhanced the counting statistics by combining physically equivalent data points acquired by different detector pixels, without introducing any noticeable error. The recorded neutron intensities, first normalized by the amount of proton charge hitting the spallation target, were then compared against measurements of a vanadium standard sample using exactly the same spectrometer conditions, to convert the intensities to absolute scattering cross-section units[37]. The resultant cross-sections were further corrected for neutron absorption, which is estimated to cause a minimum of 22% reduction of the scattering intensity based on tabulated data[38], $E_i=28$ meV, and an effective sample thickness of 18 mm. The absorption-corrected absolute cross-sections are presented throughout the paper.

LSWT fitting and simulations. Although the collinear antiferromagnetic ground state of Cu_3TeO_6 can be readily understood by considering only the antiferromagnetic nearest-neighbour exchange interactions (Fig. 1a), spin interactions over longer distances turn out to be necessary for describing the observed spin excitations. To handle the workload of searching a large parameter space and avoid local minima in the optimization process, we employ a two-step method, namely, first fitting the dispersion $\omega_m(\mathbf{q})$ extracted by data inspection to estimate the effective interactions, and then fitting the entire intensity patterns starting from the preliminary interactions. We model the effective spin interactions as:

$$H=H_{1\mathrm{NN}}+H_{2\mathrm{NN}}+\cdots H_{M\mathrm{NN}}=\sum_{d=1}^{M}J_d\sum_{i,j\in d\mathrm{NN}}\mathbf{S}_i\cdot\mathbf{S}_j$$

where J_d is the Heisenberg exchange interaction between the dth-nearest neighbours.

For the first step of our model optimization, once the number of interactions (M) and their strengths are chosen, standard Holstein–Primakoff transformation is performed, and the magnon dispersions are obtained after a straightforward calculation[15]. Comparing the model to the measurement results, we can first rule out the $M=2$ model. Under the notion that there are a total of six observed magnon branches (Figs. 2 and 3), the optical branches meet at a two-fold and a three-fold degenerate energy point at the Γ-point of the BZ, with the two-fold degenerate energy ($E_{\Gamma,2}$) higher than the three-fold degenerate energy ($E_{\Gamma,3}$). At the H-point, the six branches meet at two energies ($E_{\mathrm{H},+}$ and $E_{\mathrm{H},-}$), both of which are three-fold degenerate. Altogether, we have $E_{\Gamma,3}<E_{\mathrm{H},-}<E_{\Gamma,2}<E_{\mathrm{H},+}$, which turns out to be incompatible with the analytical expressions of the corresponding energies calculated from the $M=2$ model:

$$E_{\Gamma,3}=\sqrt{4(-J_1+J_2)(-J_1+J_2)}\,,$$
$$E_{\Gamma,2}=\sqrt{3(-J_1+J_2)(-J_1+3J_2)}\,,$$
$$E_{\mathrm{H},\pm}=\sqrt{3J_1^2+5J_2^2-8J_1J_2\pm4|J_2(J_1-J_2)|}$$

As M is further increased, analytical expressions at high-symmetry BZ points are no longer sufficient to determine the interactions. Nevertheless, we are able to obtain the following analytical expressions for models with interactions up to J_6:

$$E_{\Gamma,3}=\sqrt{4(-J_1+J_2-J_3+J_5+J_6)(-J_1+J_2-J_4+J_5+J_6)}\,,$$
$$E_{\Gamma,2}=\sqrt{3(-J_1+J_2+J_6)(-J_1+3J_2-2J_3-2J_4+3J_6)}\,,$$
$$E^2_{\mathrm{H},\pm}=3J_1^2+5J_2^2+4J_1J_3+4J_1J_4+2(J_3-J_5)(J_4-J_5)$$
$$-4J_2(2J_1+J_3+J_4-J_5)-4J_1J_5-8J_1J_6+6J_2J_6$$
$$-4(J_3+J_4-J_5)J_6+5J_6^2\pm2\sqrt{A}$$

where

$$A=J_6^2[5J_5^2-J_5(4J_1-2J_3)+J_1(4J_1+4J_3)]$$
$$+J_4^2[(J_1+J_6)^2+(J_3+J_5)^2]+4J_2^4+4J_6^4$$
$$-2J_2J_6[2J_3(2J_1+J_4-J_5)+(2J_1+J_4-3J_5)(2J_1+J_4+J_5)]$$
$$-J_6^2(4J_1+2J_3+2J_4-2J_5)-J_5[J_1J_4-J_3(J_1+2J_4)]$$
$$-2J_5^3+J_5^2(4J_1+2J_3+2J_4)+J_1J_4(2J_1+J_3+J_4)$$
$$+J_2^2[8J_1J_4-4J_1J_5-2J_4J_5+J_6(8J_1+4J_4-4J_5)$$
$$+4J_1^2+J_4^2+5J_5^2-8J_6^2+2J_3(2J_1+J_4-J_5+2J_6)]$$
$$-J_6^3(8J_1+4J_3-4J_5)+4J_2^3(2J_1+J_3+J_4-J_5)$$
$$+2J_4[J_6^2+J_1J_6+J_5(J_3+J_5)](2J_1+J_3-J_5-2J_6)$$
$$+J_5^2(3J_1+J_3-J_5)(J_1+J_3-J_5)+2J_5J_6[2J_5^2$$
$$+(-4J_1-2J_3)J_5+J_1J_3]$$

These expressions allow us to quickly determine whether a given parameter set can reproduce the experimentally measured dispersions at Γ and H, where we have used the following criteria:

$$E_{\mathrm{H},+}>E_{\Gamma,2}>E_{\mathrm{H},-}>E_{\Gamma,3},$$
$$E_{\Gamma,3}>0.8\,E_{\Gamma,2},$$
$$E_{\mathrm{H},-}>0.8\,E_{\mathrm{H},+}$$

We are then able to quickly sample through the large six-dimensional parameter space and eliminate a large portion of it. It turns out that for the remaining regions, the calculated dispersions severely depart from the experimentally measured ones, and that the global best-fit parameters (with minimal χ^2, see below and Supplementary Fig. 3b) belong to a region that does not satisfy the above criteria. Therefore, we conclude that interactions up to J_6 are insufficient for describing our experimental dispersions.

We proceed by attempting to fit the magnon dispersions along high-symmetry momentum cuts. The high-quality INS data allow us to extract a discrete set of $\omega_m(\mathbf{q})$ points along the high-symmetry lines, as displayed in Supplementary Fig. 3a. As our main goal here is to use LSWT calculations to guide our search for topological magnon band crossing, we have purposely refrained from introducing band-crossing structures into the extracted $\omega_m(\mathbf{q})$ data, to avoid biasing the model. We then perform nonlinear least-squares fitting of the $\omega_m(\mathbf{q})$ data by the Levenberg–Marquardt method. To overcome local-minima problems in the fitting process, we have performed a systematic search by starting from a multi-dimensional grid of the initial parameter set, and used a chi-square (χ^2) test to assess the goodness of the fit obtained from each initial parameter set before a globally optimized result is obtained. We estimate a reading error of 0.2 meV on $\omega_m(\mathbf{q})$, which is used for calculating the χ^2 values presented in Supplementary Fig. 3. As has been stated in the preceding paragraph, the experimental dispersions cannot be well described by the $M=6$ model (Supplementary Fig. 3b), but the quality of the fit is much improved with $M=7$ (Supplementary Fig. 3c), which results in a parameter set that is dominated by J_1 and J_7, and which satisfies the above criteria pertaining to the energies at Γ and H. However, structural considerations indicate that the exchange pathway of J_9 is even more favourable for a strong interaction than that of J_7 (see Fig. 1b and Supplementary Fig. 5, as well as Supplementary Table 1). Therefore, we have further extended the model to $M=9$. Indeed, not only do we find that the $M=9$ model is more likely to converge to parameters dominated by J_1 and J_9, but the fit quality is noticeably improved with χ^2 becoming close to unity (Supplementary Fig. 3d,e). Thus, we conclude that the $M=9$ model dominated by J_1 and J_9 is the most suitable description of the spin interactions in Cu_3TeO_6. This result is very different from all previous understandings of the spin-interaction network of this compound[17,18,32,39], can be substantiated by first-principles calculations (O. Janson, personal communication) and is beyond the analysis employed in ref. [31].

Although the $M=9$ Heisenberg model successfully describes the optical magnon dispersions, a noticeable discrepancy from the experimental data is the lack of a low-energy excitation gap at the BZ centre. This is expected because the antiferromagnetic order breaks the continuous SU(2) symmetry, which guarantees that the low-energy excitations are gapless Goldstone modes. A physically

rigorous remedy to this discrepancy is to introduce site-dependent exchange anisotropy that respects the crystal symmetry, such as Dzyaloshinsky–Moriya interactions[15,40], since spin-1/2 systems (which would be the case for Cu^{2+} in the absence of spin–orbit coupling) cannot have single-ion anisotropy, and because the cubic (or tetrahedral) crystal symmetry of Cu_3TeO_6 is incompatible with any global magnetic easy axis. However, the presence of such site-dependent exchange anisotropy generally favours a non-collinear magnetic structure, which significantly complicates the LSWT calculations. Meanwhile, neutron powder diffraction results indicate that the magnetic order in Cu_3TeO_6 is predominantly collinear, with possible non-collinear canting of the spins being no more than 6° (ref. [17]); moreover, our INS data suggest that all magnons are two-fold degenerate (6 instead of 12 branches), which indicates that the magnetic ground state is approximately collinear. Therefore, we believe that the experimentally observed anisotropy gap can be accounted for by introducing a phenomenological global single-ion anisotropy term $H_a = -D(S_i^z)^2 (D>0)$, without affecting the description of the optical branches. For the $M=9$ model, this term leads to a gap at the Γ-point, $\Delta = \frac{1}{2}\sqrt{D(8J_1+4J_3+4J_5+8J_7+8J_9+D)}$. Indeed, Supplementary Fig. 3f shows that the successful description of the optical magnon dispersions remains intact after the anisotropy gap has been accounted for, and the best-fit parameters after introducing this anisotropy are very similar to those in the Heisenberg model (Supplementary Table 1). We note that such global single-ion anisotropy does not break the U(1) symmetry; hence, our anisotropic model still results in Dirac-point-like band crossings rather than nodal rings, which are generally expected with the more realistic site-dependent exchange anisotropy[15]. However, given the very small effect of the single-ion anisotropy term on the optical magnon dispersions, we believe that the exchange anisotropy in Cu_3TeO_6 would not lead to any observable consequences in the optical magnon dispersions either.

In the second step of our optimization, our goal is to describe the measured INS intensity. To obtain the excitation spectra at any general $\mathbf{Q}$ and ω using a given parameter set of the $M=9$ model with global single-ion anisotropy, we calculate

$$S^{\alpha\beta}(\mathbf{Q},\omega) = \frac{1}{2\pi}\int_{-\infty}^{\infty} \mathrm{d}t\ \mathrm{e}^{-i\omega t} \sum_l \mathrm{e}^{i\mathbf{Q}\cdot\mathbf{r}_l} \langle S_0^{\alpha}(0) S_l^{\beta}(t)\rangle$$

which can be converted into absolute scattering cross-section units:

$$\frac{k}{k'}\frac{\mathrm{d}^2\sigma}{\mathrm{d}\Omega \mathrm{d}E} = \frac{N}{\hbar}\left(\frac{\gamma r_e}{2}\right)^2 g^2\, |F(\mathbf{Q})|^2\, \mathrm{e}^{-2W(Q)} \sum_{\alpha\beta}(\delta_{\alpha\beta} - Q_\alpha Q_\beta) S^{\alpha\beta}(\mathbf{Q},\omega)$$

where N is the number of primitive cells in the sample, $\left(\frac{\gamma r_e}{2}\right)^2 = 72.65\times10^{-3}$ barn, $g\,(=2)$ is the Landé splitting factor, and α and β are indices (xyz) of a Cartesian coordinate system[41]. For simplicity, we assume the Debye–Waller factor $\mathrm{e}^{-2W(Q)}$ to be unity, and calculate the magnetic form factor $F(\mathbf{Q})$ in the isotropic approximation (for our measured momentum region, $|F(\mathbf{Q})|^2$ amounts to about 0.75). To reproduce the measured INS spectra, we perform the same $\mathbf{Q}$-space folding of the calculated $S(\mathbf{Q},\omega)$ and use $\langle 1-Q_\alpha^2\rangle_{\mathrm{domain}} = \frac{2}{3}$, both of which account for the presence of multiple antiferromagnetic domains in our sample[17,40] and the fact that the neutron beam is not spin-polarized. A global harmonic oscillator damping to the magnons has been introduced, so that the calculated magnon intensities have a finite energy width rather than being delta-function-like singularities[42]. In addition, we introduce a global coefficient to the calculated intensities, to account for possible reduction of the coherent magnon signals caused by, for example, quantum fluctuations.

We use the intensity patterns from 13 to 19.5 meV in Supplementary Fig. 3a as the target of our optimization, to concentrate on the optical branches. Our fitting involves a total of 12 free parameters: the effective spin interactions (J_1, J_2 …, J_9), anisotropy (D), damping and global intensity coefficient. We use the preliminary results from the first step as initial values of the former ten parameters, and all parameters are simultaneously adjusted to minimize the χ^2 deviation of the calculated intensities from the measured ones. The statistical uncertainty (1 s.d.) of the measured intensities is used as variance for the calculation of χ^2.

As shown in Supplementary Table 1, the fit converges to parameters with a modest change in the interaction and anisotropy energies. The intensity coefficient reads 0.872 ± 0.006 for $g=2$. The presented calculated intensities have been adjusted accordingly throughout the manuscript. The global agreement between the calculated and the measured spectra is very good, with $\chi^2 = 7.2$ in spite of the very small statistical errors in our data that are used for the calculation of χ^2. Importantly, the LSWT simulation successfully reproduces most of the rather complicated details in $S(\mathbf{Q},\omega)$ contained in the many gigabytes of INS data of our measurement (Fig. 3), and the global standard deviation is within 10% of the maximum intensity. Finally, to assess the convergence property of our fitting method, we have run test fits starting from interaction and anisotropy parameters that are purposely set different from the preliminary results from the first step. As long as the deviation is within 20%, the fit always converges to the same result.

Using the fully optimized parameters of the LSWT model, we have calculated the ordered moment magnitude, by accounting for the reduction to the moment size due to zero-point motions of the magnons, to be $0.85\,\mu_B$ per Cu^{2+} for $g=2$. This value is considerably larger than the expected value ($0.60\,\mu_B$) in a two-dimensional square lattice[43], and is very close to that ($0.83\,\mu_B$) in a body-centred cubic lattice[44] that has the same coordination number ($N=8$) as the magnetic lattice of Cu_3TeO_6. The LSWT-calculated ordered moment magnitude for Cu_3TeO_6 is greater than the value of $0.64\,\mu_B$ per Cu^{2+} reported previously based on neutron diffraction measurement[17]. We note that the LSWT prediction on the dynamic spectral weight departs less (by 13%) from our experimental value than the departure (by 76%) of the calculated diffraction intensity (proportional to the ordered moment squared) from the previous experimental result[17].

Topological surface states. An important consequence anticipated from the non-trivial band topology in the bulk is the associated surface states, as ensured by the bulk-edge correspondence principle for topological matter. We consider a typical open surface of the (001) crystallographic plane, and calculate the dynamic susceptibility on the surface, using Green's function of the spin-wave field as explained in ref. [15]. The resultant broad features and sharp lines indicate bulk and surface magnon excitations, respectively (Supplementary Fig. 10a,c–e). The sharp lines are then picked up numerically throughout the surface Brillouin zone, to simulate the surface magnon density of states in comparison to that of the bulk states (Supplementary Fig. 10b,f). The different energy distributions of these two types of magnon suggest that an INS experiment with sufficiently good energy resolution might be able to differentiate them in a fine-powder sample, which has a significantly larger surface-layer volume compared to single crystals.

Data availability. The data that support the plots within this paper and other findings of this study are available from the corresponding authors upon reasonable request.

References

32. He, Z. & Itoh, M. Magnetic behaviors of Cu_3TeO_6 with multiple spin lattices. *J. Mag. Mag. Mater.* **354**, 146–150 (2014).
33. Kajimoto, R. et al. The Fermi chopper spectrometer 4SEASONS at J-PARC. *J. Phys. Soc. Jpn* **80**, SB025 (2011).
34. Nakamura, M. et al. First demonstration of novel method for inelastic neutron scattering measurement utilizing multiple incident energies. *J. Phys. Soc. Jpn* **78**, 093002 (2009).
35. Inamura, Y., Nakatani, T., Suzuki, J. & Otomo, T. Development status of software "Utsusemi" for chopper spectrometers at MLF, J-PARC. *J. Phys. Soc. Jpn* **82**, SA031 (2013).
36. Ewings, R. et al. HORACE: software for the analysis of data from single crystal spectroscopy experiments at time-of-flight neutron instruments. *Nucl. Instrum. Meth. A* **834**, 132–142 (2016).
37. Xu, G., Xu, Z. & Tranquada, J. M. Absolute cross-section normalization of magnetic neutron scattering data. *Rev. Sci. Instrum.* **84**, 083906 (2013).
38. Shirane, G., Shapiro, S. M. & Tranquada, J. M. *Neutron Scattering with a Triple-Axis Spectrometer: Basic Techniques* (Cambridge Univ. Press, Cambridge, 2002).
39. Choi, K. Y., Lemmens, P., Choi, E. S. & Berger, H. Lattice anomalies and magnetic excitations of the spin web compound Cu_3TeO_6. *J. Phys. Condens. Matter* **20**, 505214 (2008).
40. Herak, M. Cubic magnetic anisotropy of the antiferromagnetically ordered Cu_3TeO_6. *Solid State Commun.* **151**, 1588–1592 (2011).
41. Lorenzana, J., Seibold, G. & Coldea, R. Sum rules and missing spectral weight in magnetic neutron scattering in the cuprates. *Phys. Rev. B* **72**, 224511 (2005).
42. Wang, M. et al. Spin waves and magnetic exchange interactions in insulating $Rb_{0.89}Fe_{1.58}Se_2$. *Nat. Commun.* **2**, 580 (2011).
43. Sandvik, A. W. Finite-size scaling of the ground-state parameters of the two-dimensional Heisenberg model. *Phys. Rev. B* **56**, 11678–11690 (1997).
44. Schmidt, R., Schulenburg, J., Richter, J. & Betts, D. D. Spin-1/2 J_1–J_2 model on the body-centered cubic lattice. *Phys. Rev. B* **66**, 224406 (2002).